On the calibration of a multistatic scattering matrix measured by a fixed circular array of antennas

Amelie Litman, Jean-Michel Geffrin, Hervé Tortel

Progress In Electromagnetics Research, Vol. 110, 1–21, 2010

ON THE CALIBRATION OF A MULTISTATIC SCATTERING MATRIX MEASURED BY A FIXED CIRCULAR ARRAY OF ANTENNAS

A. Litman, J.-M. Geffrin, and H. Tortel

Institut Fresnel, Universite Aix-Marseille
CNRS, Ecole Centrale Marseille Campus de St Jérôme
Marseille Cedex 13397, France

Abstract—The calibration of the multistatic scattering matrix plays an important part in the construction of a quantitative microwave imaging system. For scattering measurement applications, the calibration must be performed on the amplitude and on the phase of the fields of interest. When the antennas are not completely identical, as for example with a multiplexed antennas array, a specific calibration procedure must be constructed. In the present work, we explain how a complex calibration matrix can be defined which takes advantage of the geometrical organization of the antennas. Indeed, for arrays of antennas positioned on a circle, the inherent symmetries of the configuration can be fully exploited by means of an adequate reorganization of the multistatic scattering matrix. In addition, the reorganization permits to detect antenna pairs which are not properly functioning and to estimate the signal-to-noise ratio. Experimental results obtained within a cylindrical cavity enclosed by a metallic casing are provided to assess the performance of the proposed calibration procedure.This calibration protocol, which is described here in detail, has already been applied to provide quantitative images of dielectric targets [1, 2].

1. INTRODUCTION

In harmonic scattering imaging procedures, the use of a large variety of illumination angles and receiving angles is of interest for filling the Ewald sphere. Indeed, in microwave tomography, a simple Fourier transforms of the Ewald sphere already provides important pieces of

Received 3 September 2010, Accepted 29 October 2010, Scheduled 6 November 2010
Corresponding author: Amelie Litman (amelie.litman@fresnel.fr).

information on the illuminated scene. Higher resolution images as well as quantitative ones can be afterwards obtained from iterative schemes. In all these imaging schemes, the entry point is thus the scattering matrix which must be as complete as possible to capture the entire scattering process.

A multistatic scattering matrix can be measured in various ways. One way is to construct it mechanically by moving physically the emitters and the receivers all around the illuminated zone. This is what has been done in a free space environment [3–5], in a liquid environment [6, 7] or above a buried target [8, 9] for example. Another possibility is to construct it electronically with a fixed array of antennas, each pair of emitter/receiver being selected thanks to hyperfrequency switches or any kind of multiplexer/demultiplexer devices, e.g., [10–15]. It is even possible to combine the two approaches as done for example in [16] where an array of modulated receivers is kept fixed and the multiple illuminations are created by rotating the target on itself.

In all setups, the calibration is of great importance. In the antenna measurement field of activities, only the measured field, and more specifically its amplitude, is of interest as the investigated object is an active one. For scattering measurement applications, the phase as well as the amplitude of the scattered field are valuable. Roughly speaking, the phase will bring information on the shape of the illuminated targets as the amplitude will help to quantify the permittivity values. But the scattered field is not measured directly as it is obtained by subtracting the field measured without the target (the incident field) from the field measured with the target (the total field). Therefore, the preliminary choice is to decide if the calibration procedure has to be applied to the measured fields or to the scattered field directly.

For a free space configuration and for elongated targets, it appeared that it is sufficient to perform calibration on the incident field itself [4] even to obtain quantitative information on the target under test. When the targets become more complex and in particular when they have a full three-dimensional structure, the calibration on the incident field is not fully satisfactory. In that case, another procedure is directly applied to the scattered field with the use of a reference target [17–19]. This is coupled with the fact that the incident field cannot be measured and/or computed with a sufficiently high precision to perform a stable calibration procedure. Indeed, even up-to-date modelling techniques are sometimes not sufficient to properly take into account cross-talks effects and radiation patterns variations due to the surrounding environment. The more the incident field will be oscillating, the more difficult it will be to obtain a good agreement

between the measurements and the simulations.

When the multistatic matrix is obtained from mechanical movements, the emitting (resp. receiving) antenna is keeping the same radiation pattern. Different calibration processes have been proposed, enabling full polarization corrections by means of distortion polarization matrices [20–22]. In other cases, a single complex coefficient turns out to be sufficient to perform an efficient calibration [17, 18], this coefficient depending only on the frequency, on the emitter's position and on the amplitude of the measured fields. Due to the time spent in the mechanical movements, this coefficient can also be corrected for drift phenomena [23].

When the multistatic matrix is obtained, as considered herein, with an antennas array combined with electronic switches, the antennas are not completely identical and a different calibration procedure should be constructed. One possibility would be to directly calibrate each antenna using a two-port calibration technique as it is done in [15], but due to our low-cost multiplexer, we are faced with too many losses which prevent us from applying this technique. Moreover, this two-port calibration technique is not sufficient to take care of the antennas diversity and the scattering phenomena. Following [17], we prefer to exhibit a single complex coefficient for each pair of emitter/receiver antennas, assuming that the antennas are all emitting/receiving with the same polarization. This produces a calibration matrix which enables to take into account the various antennas behaviors which can also differ from the emission mode to the reception mode.

In [11, 14], such a calibration matrix is computed by dividing each measured scattered field by a coefficient which corresponds to the ratio between the measured incident field and the simulated incident field for each pair of antenna/receiver. This calibration technique does not ensure nevertheless that the field at the target location will be indeed similar to the field that will be simulated there, leading to unsatisfactory calibrated fields as encountered in [14]. To better ensure this, it is more appropriate to compute the calibration matrix by dividing each measured scattered field with a coefficient which corresponds this time to the ratio between the scattered field measured for a given reference target and its associated simulated field. This technique has been employed in [10, 24].

This technique is neverless not sufficient to fully take into account the diversity in terms of emitter and receiver illuminations and the fact that all antennas might have measurement errors which must be accounted for. We thus propose to construct the calibration matrix keeping in mind that each row corresponds to the same emitting

antenna, while each column corresponds to the same receiving antenna. The only restriction being made here resides in the fact that the multistatic antennas array is arranged in a circular manner, that is, that the antennas are placed on a circle surrounding the target and that they all emit with the same polarization. This geometrical feature is fully exploited through a reorganization of the multistatic scattering matrix which highlights the inherent symmetries of the configuration. This calibration protocol has successfully been applied before to provide quantitative images of dielectric targets [1, 2], but it was never described in detail.

The present work explains how a fixed array of antennas can be calibrated for scattering imaging purposes. The article is organized as follows. The first section describes the measurement apparatus for which the calibration procedure was first proposed. The calibration procedure is then detailed in the second section. A short conclusion follows.

2. EXPERIMENTAL SETUP

2.1. Geometrical Arrangement

The microwave scanner for which the calibration procedure has been at first implemented consists in a cylindrical cavity enclosed in a metallic casing. This setup is one of the various microwave imaging setups that Institut Fresnel is developing. It was first constructed at Laboratoire des Signaux et Systèmes for hyperthermia monitoring applications [12]. The enclosing metallic boundary protects from external microwave perturbations. In comparison with a free space environment and as long as the antennas are correctly positioned with respect to this highly conductive barrier, it also increases the energy level which can penetrate an object placed at the center of the measurement setup [25].

Its particularity, apart from the external metallic boundary, resides in the fact that the entire cavity is filled with water (Figure 1). Water was chosen for improving the impedance matching between the external medium where the antennas radiate and the object to image. For biomedical applications, water [26] or glycerin [27] are commonly used. For a similar cavity, but filled with air and currently under construction, one can refer to [14, 24].

Another of its particularities resides in the presence of an array of 64 identical antennas (Figure 1). These antennas are mounted in the same horizontal plane, on a circle of slightly smaller radius ($R_\Gamma = 27.6\,\mathrm{cm}$) than the metallic border ($R_\Sigma = 29.5\,\mathrm{cm}$). They are angularly equally spaced and immersed in the embedding liquid.

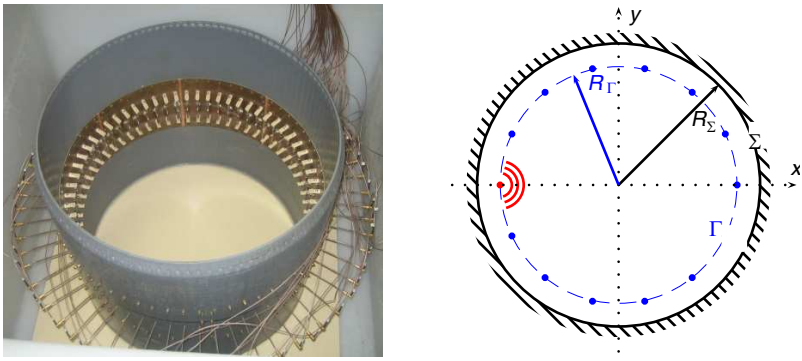

(a) (b)

Figure 1. Picture and cross-sectional sketch of the microwave scanner.

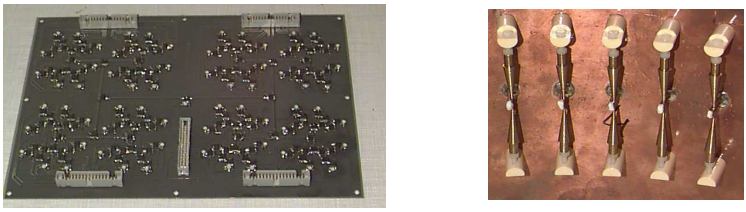

(a) (b)

Figure 2. (a) One rack of the multiplexer/demultiplexer device. (b) Biconical antennas which are designed to radiate a $E\|$ linearly polarized field within water at 434 MHz.

2.2. Measurement Apparatus

The measuring equipment is based on a Vector Network Analyser (VNA) (Anritsu 64xx). This VNA is connected to a hyperfrequency multiplexer/demultiplexer which is working in a $1 \rightarrow 64/64 \rightarrow 1$ mode (Figure 2(a)). The antennas are all connected to this home-made multiplexer/demultiplexer device. These antennas are biconical antennas [12] whose characteristic dimensions (with a cone angle of 15° and a height of 26 mm for each cone) have been specifically designed to radiate at 434 MHz inside water (Figure 2(b)). They are assumed to radiate the same $E\|$ linearly polarized field. The entire system is controlled via a PC and a home-made monitoring software, written in C. To perform an acquisition of a multistatic scattering matrix with 63×64 terms, the overall measurement time is about 30 min, if no specific rapidity is required.

2.3. Measurement Protocol

The measurement protocol consists in four consecutive steps. First of all, the incident field measurement E_i^{meas} is performed. One antenna is selected as the emitting antenna, while the 63 remaining ones are set in the receiving mode. The amplitude and the phase of the field are then measured sequentially for each of the 63×64 pairs. Secondly, the total field measurement for the reference target $E_{t,ref}^{meas}$ is performed, taking care that the embedding liquid is always at the same level of 59 cm as for the incident field measurement. Thirdly, the reference target is removed, the unknown target is positioned inside the scanner and the total field measurement E_t^{meas} is performed, with again the same level of the embedding liquid as for the incident field measurement. Finally, the permittivity of the embedding liquid is measured thanks to a coaxial open-ended probe directly connected to the network analyzer [28]. This last step provides the value of the permittivity with the same experimental conditions as the rest of the measurements.

The scattered field of the reference $E_{d,ref}^{meas}$ (resp. unknown E_d^{meas}) target is then obtained by subtracting the incident field from the reference (resp. unknown) total field measurement for each emitting antenna r_e and receiving antenna r_r couple. The scattering matrices $\mathbb{K}_{d,ref}^{meas} = \{E_{d,ref}^{meas}(r_e, r_r)\}$ and $\mathbb{K}_d^{meas} = \{E_d^{meas}(r_e, r_r)\}$ are then easily constructed.

3. CALIBRATION PROCEDURE

The calibration procedure is necessary for several purposes. First of all, the channels in the multiplexer device are not rigorously identical. Moreover, the input and output lines are not shared. This introduces signal variations when the same antenna is used in an emission mode or in a reception mode. Secondly, it enables to perform not only qualitative but also quantitative measurements [17]. Thirdly, it enables to detect the antennas which are not properly working during the acquisition time. Indeed, due to bubbles in water and due to corrosion at the soldered parts of the antennas, the antennas are sometimes not properly functioning. This is an important piece of information for the inversion procedure, as the non-working antenna pairs can then be easily removed from the processing. Finally, it permits to estimate the signal to noise ratio of the apparatus.

The calibration procedure ends in the definition of a calibration matrix $\mathbb{C} = \{C(r_e, r_r)\}$. The calibrated scattered field for the unknown

target is obtained by applying this calibration matrix as follows

$$E_d^{meas,cal}(r_e, r_r) = E_d^{meas}(r_e, r_r)/C(r_e, r_r), \quad \forall(r_e, r_r) \tag{1}$$

which can be synthesized by introducing the element-by-element division operation $(\cdot/)$, that is,

$$\mathbb{K}_d^{meas,cal} = \mathbb{K}_d^{meas} \cdot / \, \mathbb{C} \tag{2}$$

A very simple calibration procedure would be to directly define the calibration matrix as in [10, 24] such that

$$C(r_e, r_r) = E_{d,ref}^{meas}(r_e, r_r)/E_{d,ref}^{sim}(r_e, r_r), \quad \forall(r_e, r_r) \tag{3}$$

where $E_{d,ref}^{sim}$ is the simulated scattered field for the reference target. But this type of calibration does not take into account the fact that the antennas have fixed positions and that they play a part at several places in the scattering matrix. Moreover, with such a calibration technique, it is not possible to determine properly the signal to noise ratio. Thus, another procedure for the determination of the matrix $\mathbb{C}$ is detailed afterwards and its flowchart is provided in Figure 3.

3.1. Fields Modelling

The calibration of the measurements are made according to a given simulation tool, which is needed in particular for the computation of $E_{d,ref}^{sim}$, the simulated scattered field for the reference target. Several algorithms have already been implemented to compute the field in this specific configuration, all of them being based on the method of moments with various types of Green functions [12, 29, 30]. Here, we prefer to use a finite element method (FEM) with conformal meshing adapted to the casing configuration [1, 2, 13]. It requires typically about 6 seconds of run time on a standard computer, for a first-order triangular mesh with 45 000 nodes and for 64 emitting antennas. Comparisons with the method of moments and with the measured fields have shown a very good agreement [31]. The antennas are simply modelled as infinitely long line sources.

3.2. Symmetry and Neighboring Storage

The reference target is a metallic circular cylinder, with a 90 mm diameter and a height of 60 cm, which has been chosen for its completely symmetrical shape and its non dielectric properties in order not to be bothered with a precise definition of its permittivity value. Moreover, the reference target can precisely be positioned at the center

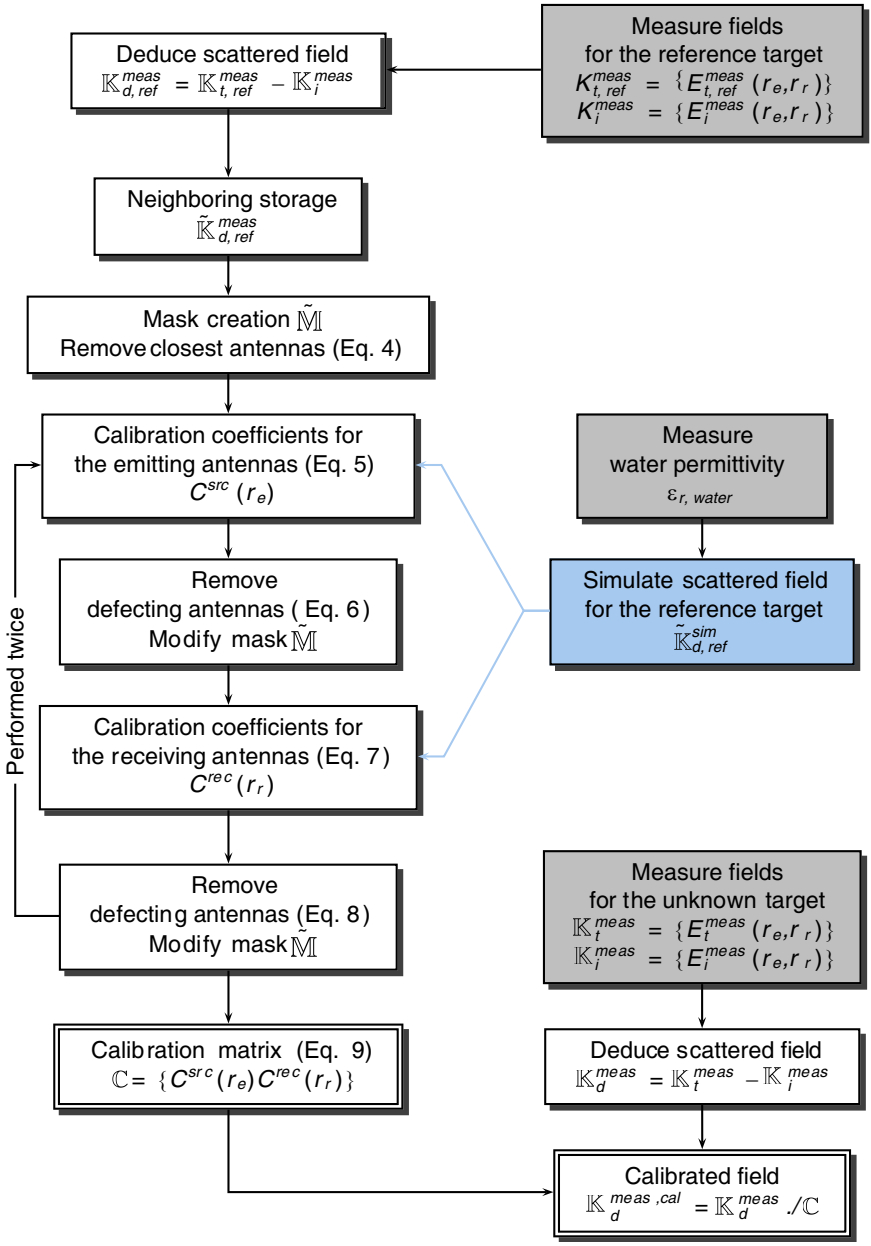

Figure 3. Flowchart of the calibration procedure.

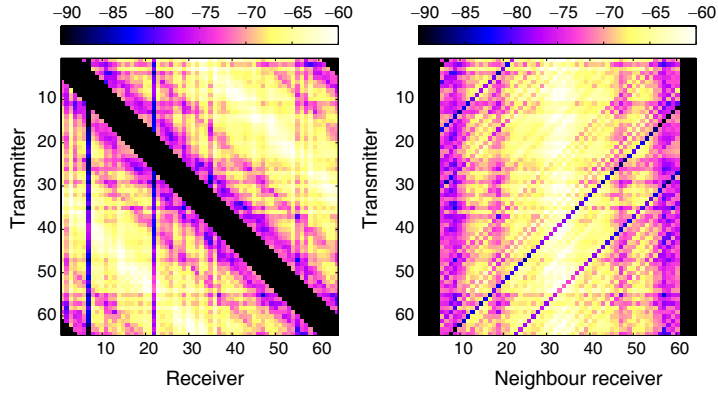

Figure 4. (a) Amplitude in dB of the scattering matrix $\mathbb{K}^{meas}_{d,ref}$. (b) Amplitude in dB of the by-neighbor scattering matrix $\tilde{\mathbb{K}}^{meas}_{d,ref}$.

of the setup in order to exploit the various symmetries (the circular cavity, the circular antenna ring, the circular reference target).

To directly visualize the symmetries and to facilitate the calibration procedure, the scattering matrix is reorganized thanks to a circular shifting. The permutation $\tilde{r}_r = p(r_e, r_r)$ is constructed such that the emitting antenna is always stored in the first column of the by-neighbor matrix $\tilde{\mathbb{K}}^{meas}_{d,ref} = \left\{E^{meas}_{d,ref}(r_e, \tilde{r}_r = p(r_e, r_r))\right\}$. The subsequent columns are now corresponding to the adjacent antennas when going in the clockwise direction (Figure 4). A similar reverse shifting procedure is applied for retrieving the classically stored scattering matrix from the by-neighbor scattering matrix.

This neighboring storage enables to directly detect if the target is exactly at the center of the setup. Indeed, due to the various symmetries, all the rows should be identical if everything was perfectly aligned. This effect is easily visible by comparing Figure 4(b) where the target is centered with Figure 11(a) where the target is off-centered. This symmetry is of great importance as we will check afterwards that the response for any emitting antenna is always the same for a given neighbour, wherever the emitting antenna is positioned.

3.3. Mask Creation

To be less sensitive to antennas cross-talks, we directly remove the n receiving antennas nearest to the emitting antenna. This directly corresponds to removing the first and the last n columns of the by-

neighbor scattering matrix $\tilde{\mathbb{K}}^{meas}_{d,ref}$. In the present case, we have taken $n = 2$. Instead of effectively removing them and in order to be able to go back easily to the classical scattering matrix, we prefer to introduce a binary mask $\mathbb{M} = \{M(r_e, r_r)\}$ such that

$$M(r_e, r_r) = \begin{cases} 1, & \text{if the antenna pair is correctly working,} \\ 0, & \text{otherwise.} \end{cases} \tag{4}$$

This mask will be updated at each step of the calibration protocol. Similarly, during the calibration process, the mask will always be applied to neglect the defective antennas.

3.4. Detecting the Defective Emitting Antennas

To determine the antennas which are not properly working when they are set in an emitting mode, we compare the behavior of the various rows of the by-neighbor scattering matrix. To that end, we compute the calibration coefficient that should be applied to each row separately, such that the simulated field matches both in amplitude and in phase to the associated measured field, at least in an average way. The calibration coefficient is therefore defined by

$$C^{src}(r_e) = \arg\min_{C} \parallel \left[\left(\tilde{\mathbb{K}}^{meas}_{d,ref} - C\tilde{\mathbb{K}}^{sim}_{d,ref} \right) \cdot * \tilde{\mathbb{M}} \right] (r_e, \cdot) \parallel^2 \tag{5}$$

where $(\cdot *)$ denotes the element-by-element multiplication operator. These calibrations coefficients are then stacked into a calibration matrix $\mathbb{C}^{src} = \tilde{\mathbb{C}}^{src} = \{C^{src}(r_e)\}$, $\forall (r_e, r_r)$ (Figure 5). If an antenna is

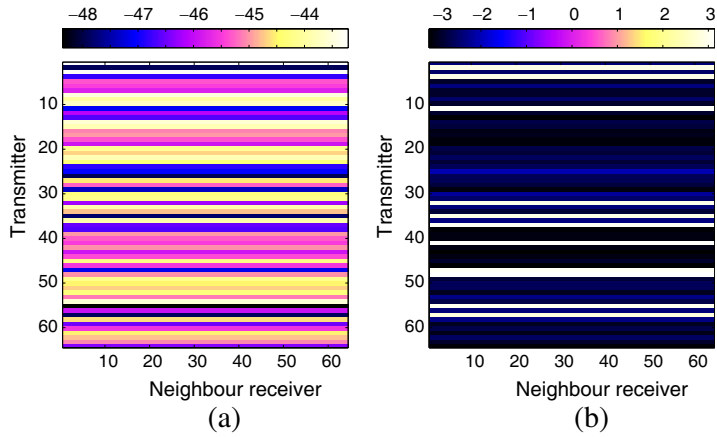

Figure 5. (a) Amplitude of the source calibration matrix $\tilde{\mathbb{C}}^{src}$. (b) Phase of the source calibration matrix $\tilde{\mathbb{C}}^{src}$.

not properly working, its associated calibrations coefficients should be different from the other calibrations coefficients. The first statistical moments of the amplitude of the calibrations coefficients are thus computed, that is, the mean $\overline{|C^{src}|}$ and the standard deviation $\sigma_{|C^{src}|}$. A defective antenna will then be detected if its associated calibration coefficient is too different from the other calibrations coefficients

$$M(r_e, r_r) = \begin{cases} 1, & \text{if } \left||C^{src}(r_e)| - \overline{|C^{src}|}\right| \leq \alpha\sigma_{|C^{src}|} \\ 0, & \text{otherwise.} \end{cases} \tag{6}$$

where α is a tuning parameter. When α is large, all emitters will be selected as working ones, when α is becoming smaller, the selection will be restricted. Here, α was set to 2, which corresponds to withdraw more or less 5% of the points. The detection of the defective emitting antennas automatically changes the mask $\mathbb{M}$ (Figure 7(a)).

3.5. Detecting the Defective Receiving Antennas

An antenna can also be mute when set in a receiving mode. The same procedure as previously described for detecting the defective emitting antennas can be applied. But this time, the procedure is applied to the standard matrix $\mathbb{K}^{meas}_{d,ref}$ and not to the by-neighbor matrix. Indeed, the columns of the reorganized matrix are not involving the response of the same receiver, but the response of all the receivers. To examine a unique receiver, one needs to refer to the standard organization. We again compute the calibration coefficient that should be applied this time to each column separately, such that

$$C^{rec}(r_r) = \arg\min_{C} \left\| \left[\left(\mathbb{K}^{meas}_{d,ref} - C\mathbb{K}^{sim}_{d,ref} \right) \cdot * \mathbb{M} \right] (\cdot, r_r) \right\|^2 \tag{7}$$

These calibrations coefficients are also stacked into a calibration matrix $\mathbb{C}^{rec} = \{C^{rec}(r_r)\}$, $\forall(r_e, r_r)$, which can be stored again in a neighboring way (Figure 6).

The first statistical moments of the amplitude of the calibration coefficients are now computed and the defective receiving antennas will be detected with a similar procedure as previously described,

$$M(r_e, r_r) = \begin{cases} 1, & \text{if } \left||C^{rec}(r_r)| - \overline{|C^{rec}|}\right| \leq \alpha\sigma_{|C^{rec}|} \\ 0, & \text{otherwise.} \end{cases} \tag{8}$$

where $\overline{|C^{rec}|}$ is corresponding to the mean value and $\sigma_{|C^{rec}|}$ to the standard deviation value. Again, the mask $\mathbb{M}$ is updated (Figure 7(b)).

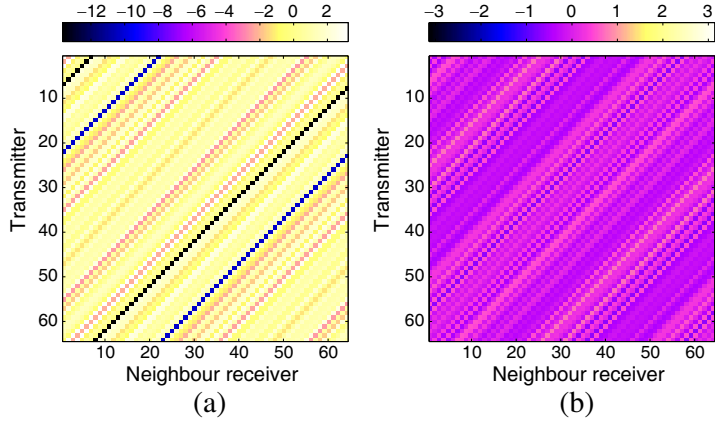

Figure 6. (a) Amplitude of the receiver calibration matrix $\tilde{\mathbb{C}}^{rec}$. (b) Phase of the receiver calibration matrix $\tilde{\mathbb{C}}^{rec}$.

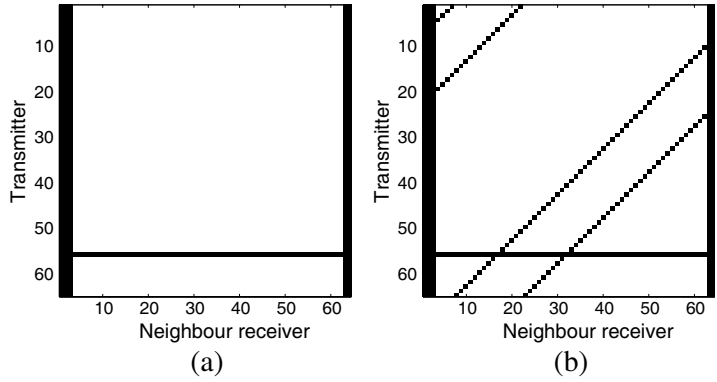

Figure 7. (a) By-neighbor mask $\tilde{\mathbb{M}}$ after the detection of the defective emitting antennas (corresponding to black lines). The $2n$ black columns are due to the elimination of the receiving antennas which are the closest ones from the emitting antenna. (b) By-neighbor mask $\tilde{\mathbb{M}}$ after the detection of the defective receiving antennas. The mute receiving antennas are corresponding to black columns in the standard $\mathbb{M}$ matrix.

3.6. Calibration Matrix

Once the unwanted pairs have been selected, the matrices $\mathbb{C}^{src}$ and $\mathbb{C}^{rec}$ are recomputed. Indeed, as the mask is changing at each step of the calibration procedure, it affects the values of the calibration coefficients. The computation/re-computation of the calibration

matrices which has been described in Section 3.5 and Section 3.5 can be performed as many times as requested if one wants to be sure to find stable calibration coefficients. In our case, two passes are fully sufficient to provide adequate calibration coefficients. The final calibration matrix is then defined as

$$\mathbb{C} = \mathbb{C}^{src} \cdot * \mathbb{C}^{rec} \tag{9}$$

3.7. Calibrated Fields

Once the calibration matrix has been derived, it can be applied to all kind of measured fields by applying (Eq. (2)). To first verify the validity of the procedure, we have compared the scattered fields for the reference target before and after the calibration, i.e., $\mathbb{K}_{d,ref}^{meas,cal} = \mathbb{K}_{d,ref}^{meas} \cdot / \mathbb{C}$, are presented in Figure 8. A complete comparison is

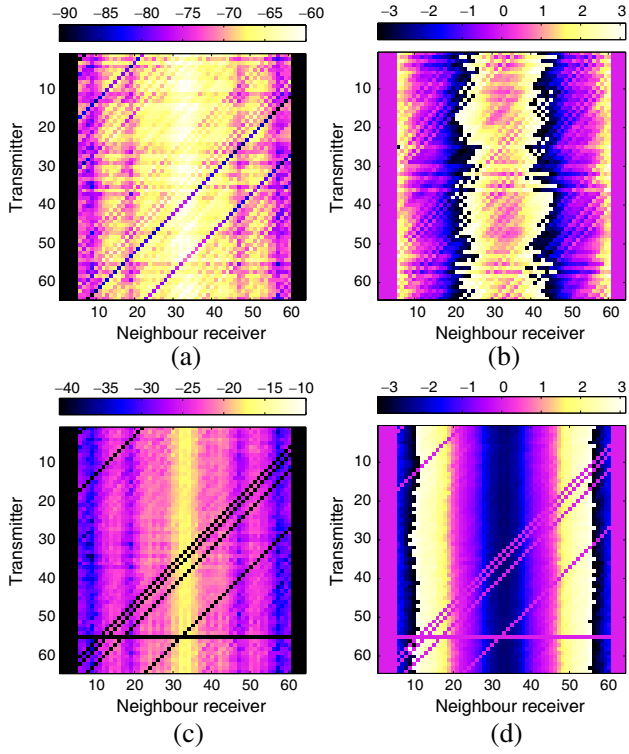

Figure 8. (a) Amplitude in dB and (b) phase of the raw scattering matrix $\tilde{\mathbb{K}}_{d,ref}^{meas}$. (c) Amplitude in dB and (d) phase of the calibrated scattering matrix $\tilde{\mathbb{K}}_{d,ref}^{meas,cal}$. The target is the reference target, a centered metallic cylinder with a 90 mm diameter.

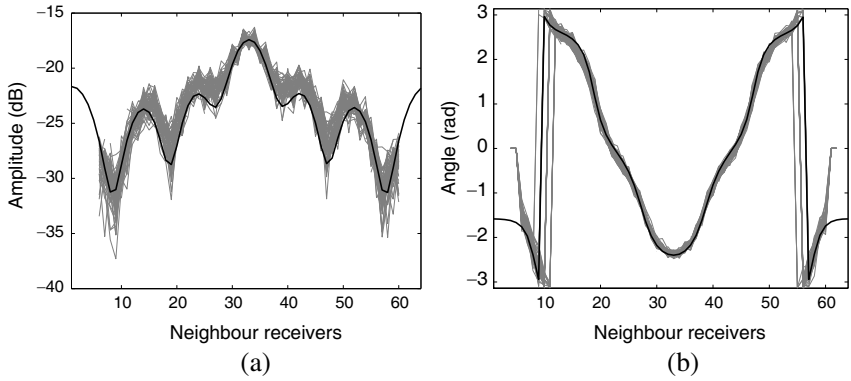

Figure 9. Amplitude (a) and phase (b) of the calibrated scattered field for the reference target, a centered metallic cylinder with a 90 mm diameter. The grey curves represent the calibrated measured field, the black curve represents the associated simulated field.

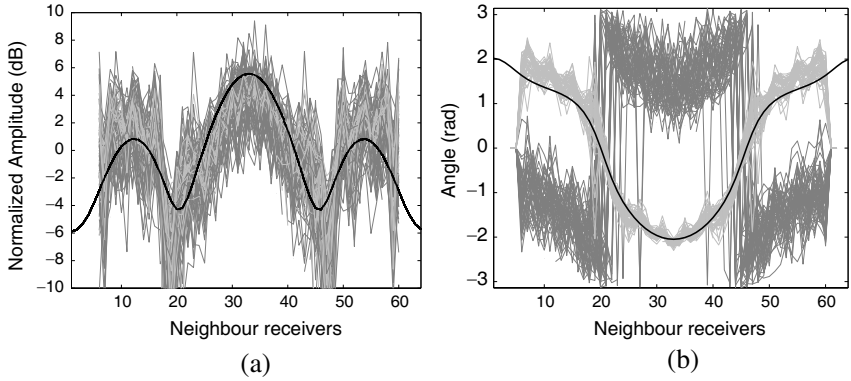

Figure 10. Normalized amplitude (a) and phase (b) of the scattered fields for an unknown target. The light grey curves represent the calibrated measured fields, the grey curves represent the raw measured fields, and the black curve represents the associated simulated field. The amplitude has been normalized by dividing each scattered field matrix by their average absolute value. The target is a centered metallic cylinder with a 60 mm diameter.

obtained by plotting for all the incidences the measured calibrated scattered field in comparison with the simulated one (Figure 9). From these figures, it is clearly visible that the calibrated fields are very close to the simulated ones, proving that the calibration is performing as expected for the reference target.

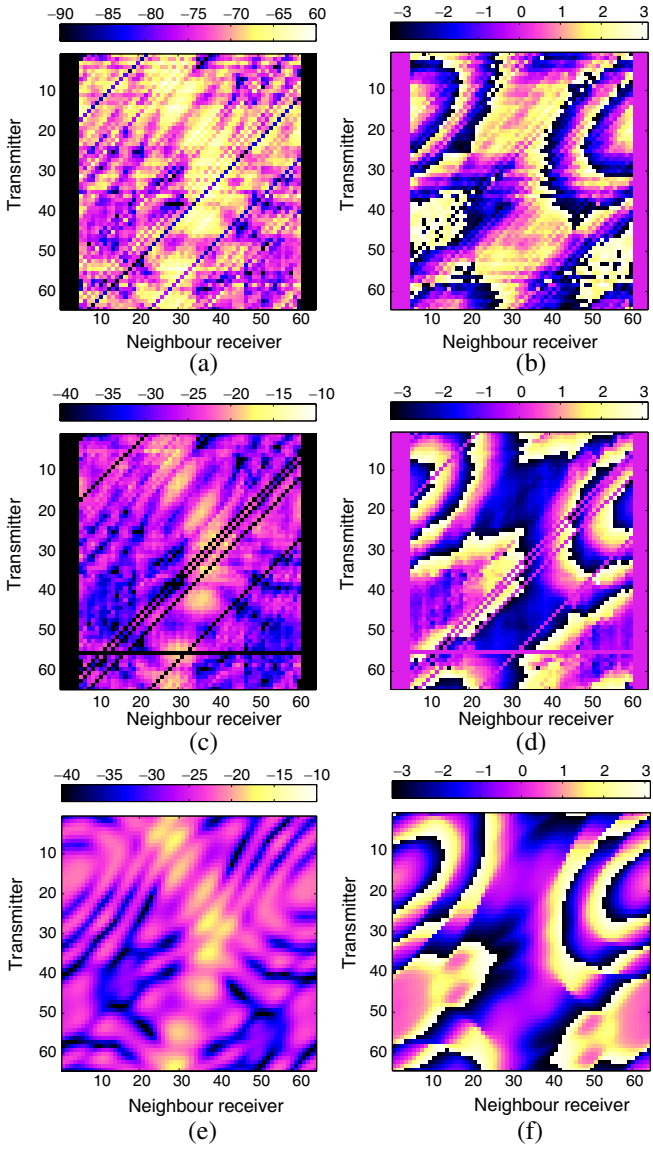

Figure 11. (a) Amplitude in dB and (b) phase of the raw scattering matrix $\tilde{\mathbb{K}}_d^{meas}$. (c) Amplitude in dB and (d) phase of the calibrated scattering matrix $\tilde{\mathbb{K}}_d^{meas,cal}$. (e) Amplitude in dB and (f) phase of the simulated scattering matrix $\tilde{\mathbb{K}}_d^{sim}$. The target is an off-centered metallic cylinder with a 60 mm diameter.

The calibration is also applied to an unknown target, in the present case a metallic cylinder with a smaller diameter of 60 mm. The same comparison between the calibrated field and the simulated one is shown in Figure 10 when the target is centered. Again, the calibration matrix enables to match the simulated field and the calibrated measured fields. Moreover, due to the fact that some antennas pairs are removed from the calibrated scattering matrix, the standard deviation of the calibrated measured field is reduced.

When the 60 mm diameter target is off-centered by 60 mm, the associated measured scattered field matrix is presented in Figure 11. Again, the two sets of plots are clearly showing a reduction of the variation ranges both in amplitude and in phase.

3.8. Estimation of the Signal to Noise Ratio

From the calibrated scattered field of the reference target, it is possible to extract information related to the signal to noise ratio of the current experiment. To that end, we compute the 1D Fourier transforms of the by-neighbor matrix $\tilde{\mathbb{K}}_{d,ref}^{meas,cal}$ with respect to the reorganized receiving angles:

$$\hat{E}_{d,ref}^{meas,cal}(r_e, \tilde{\nu}_r) = \int_{\Gamma} E_{d,ref}^{meas,cal}(r_e, \tilde{r}_r) \exp(-2i\pi\tilde{\nu}_r\tilde{r}_r) d\tilde{r}_r \tag{10}$$

We then compute the average amplitude spectrum with respect to the emitters,

$$\overline{|\hat{E}_{d,ref}^{meas,cal}|^2}(\tilde{\nu}_r) = \frac{1}{64} \sum_{r_e} \left| \hat{E}_{d,ref}^{meas,cal}(r_e, \tilde{\nu}_r) \right|^2 \tag{11}$$

As it is well-known that the scattering phenomenon is a low-pass filter with respect to the receiving angles [32], the average amplitude spectrum must have a band-limited spectrum. The high frequency components, if there are any, are therefore only due to noise. This is visible for example in the simulated scattered field spectrum whose associated numerical random noise is around 70 dB. By comparing the high-frequency parts of the measured average spectrum, it is possible to deduce the average signal to the noise ratio of the current experiment (Figure 12). In our case, we have found a signal-to-noise ratio of approximately 25 dB. This signal-to-noise ratio definitely needs to be improved. Nevertheless, interesting quantitative images have been obtained with this system for dielectric targets [1, 2].

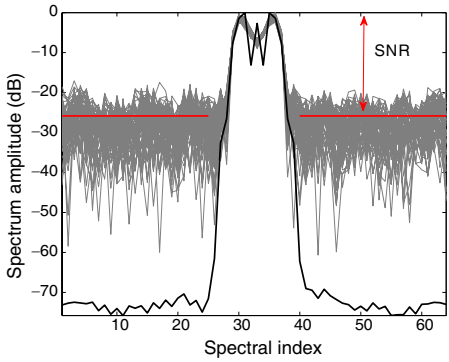

Figure 12. Amplitude in dB of the reference target scattered field spectrum computed with respect to the reorganized receiver positions. The grey curves represent the measured and calibrated scattered field spectra $\hat{E}_{d,ref}^{meas,cal}$ for the various emitters, the black curve represents the associated simulated spectrum $\hat{E}_{d,ref}^{sim}$.

4. CONCLUSION

We have provided therein an explanation of a calibration procedure which has been specifically constructed for multistatic matrices obtained from antennas which are organized in a circle all around the illuminated area. The only restriction is given by this circular geometrical arrangement of the antennas array.

This calibration has been tested in the specific configuration of a ring of antennas positioned inside a circular metallic enclosure. The validation of the entire quantitative imaging procedure is not presented in the current article, as it has been done already in other works [1, 2]. Indeed, the effective and accurate reconstructed images that have been obtained from measured data which have been calibrated as described therein, are testifying of the quality of the calibration process.

Of course, the current calibration process could and should be improved. In particular, the three-dimensional structure of the antennas is not perfectly taken into account in the modelling. These 2D/3D effects have already been shown to be non-negligible [33] and should be taken into account. The mask's creation only provides here a binary information, but we could mitigate it by replacing it with correlation matrices. This would imply the creation of a correlation matrix for each emitter and thus the mask would be replaced by a $63 \times 64 \times 64$ matrix. This correlation matrix would bring, for each emitting antenna, pieces of information on the potential cross-talks

between the receiving antennas as well as confidence weightings on each measurement. The introduction of such a correlation matrix has already been shown to be of interest for improving the spatial and quantitative resolution of the reconstructed images in a free space environment [34]. Finally, the extension of such a calibration procedure to setups where the antennas are not organized in a circular way is of great challenge, in particular for aspect-limited configurations, which will be explored in future works.

REFERENCES

1. Lencrerot, R., A. Litman, H. Tortel, and J.-M. Geffrin, "Imposing Zernike representation for two-dimensional targets imaging," *Inverse Problems*, Vol. 25, No. 3, 035012, 2009.
2. Litman, A., R. Lencrerot, and J.-M. Geffrin, "Combining spatial support information and shape-based method for tomographic imaging inside a microwave cylindrical scanner," *Inverse Problems Sci. Eng.*, Vol. 18, No. 1, 19–34, 2010.
3. McGahan, R. and R. Kleinman, "Third annual special session on image reconstruction using real data," *IEEE Antennas Propagat. Mag.*, Vol. 41, No. 1, 34–36, 1999.
4. Geffrin, J.-M., P. Sabouroux, and C. Eyraud, "Free space experimental scattering database continuation: Experimental setup and measurement precision," *Inverse Problems*, Vol. 21, No. 6, S117–S130, 2005.
5. Solimene, R., A. Brancaccio, J. Romano, and R. Pierri, "Localizing thin metallic cylinders by a 2.5D linear distributional approach: Experimental results," *IEEE Trans. Antennas Propagat.*, Vol. 56, No. 8, 2630–2637, 2008.
6. Yu, C., M. Yuan, J. Stand, E. Bressiour, R. George, G. Ybarra, W. Joines, and Q. Liu, "Active microwave imaging II: 3D systeme prototype and image reconstruction from experimental data," *IEEE Trans. Microwave Theory and Tech.*, Vol. 56, No. 4, 991–1000, 2008.
7. Duchêne, B., A. Joisel, and M. Lambert, "Nonlinear inversions of immersed objects from laboratory-controlled data," *Inverse Problems*, Vol. 20, No. 6, S81–S98, 2004.
8. Eyraud, C., J.-M. Geffrin, P. Lewyllie, A. Franchois, and A. Dubois, "Target localization and measured scattered field preprocessing using spectral bandwidth minimization for shallowly buried target problems," *Microw. Opt. Tech. Lett.*, Vol. 52, No. 1, 147–151, 2010.

9. Yu, C., M. Yuan, J. Stand, R. George, G. Ybarra, W. Joines, and Q. Liu, "Microwave imaging in a layered media: 3D image reconstruction from experimental data," *IEEE Trans. Antennas Propagat.*, Vol. 58, No. 2, 440–448, 2010.
10. Broquetas, A., J. Romeu, J. Rius, A. Elias-Fuste, A. Cardama, and L. Jofre, "Cylindrical geometry: A further step in active microwave tomography," *IEEE Trans. Microwave Theory and Tech.*, Vol. 39, No. 5, 836–844, 1991.
11. Meaney, P., M. Fanning, D. Li, S. Poplack, and K. Paulsen, "A clinical prototype for active microwave imaging of the breast," *IEEE Trans. Microwave Theory and Tech.*, Vol. 48, No. 11, 1841–1853, 2000.
12. Geffrin, J.-M., "Imagerie microonde: Etude d'un scanner a 434 MHz pour applications biomedicales," Ph.D. Thesis, University of Paris XI, Orsay, France, 1995.
13. Lencrerot, R., A. Litman, H. Tortel, and J.-M. Geffrin, "Measurement strategies for a confined microwave circular scanner," *Inverse Problems Sci. Eng.*, Vol. 17, No. 6, 787–802, 2009.
14. Mojabi, P. and J. LoVetri, "Eigenfunction contrast source inversion for circular metallic enclosures," *Inverse Problems*, Vol. 26, No. 2, 025010, 2010.
15. Padhi, S., A. Fhager, M. Persson, and J. Howard, "Measured antenna response of a proposed microwave tomography system using an efficient 3-D FFT model," *IEEE Antennas and Wireless Propag. Lett.*, Vol. 7, 689–692, 2008.
16. Azaro, R., S. Caorsi, and M. Pastorino, "A 3-GHz microwave imaging system based on a modulated scattering technique and a modified Born approximation," *Int. J. Imaging Systems Tech.*, Vol. 9, 395–403, 1998.
17. Eyraud, C., J.-M. Geffrin, P. Sabouroux, P. C. Chaumet, H. Tortel, H. Giovannini, and A. Litman, "Validation of a 3D bistatic microwave scattering measurement setup," *Radio Sci.*, Vol. 43, No. 4, RS4018, 2008.
18. Geffrin, J.-M., C. Eyraud, A. Litman, and P. Sabouroux, "Optimization of a bistatic microwave scattering measurement setup: From high to low scattering targets," *Radio Sci.*, Vol. 44, RS2007, 2009.
19. Geffrin, J.-M. and P. Sabouroux, "Continuing with the fresnel database: Experimental setup and improvements in 3D scattering measurements," *Inverse Problems*, Vol. 25, No. 2, 024001, 2009.

20. Kahny, D., K. Schmitt, and W. Wiesbeck, "Calibration of bistatic polarimetric radar systems," *IEEE Trans. Geosci. Remote Sens.*, Vol. 30, No. 5, 847–852, 1992.
21. Whitt, M., F. Ulaby, P. Polatin, and V. Liepa, "A general polarimetric radar calibration technique," *IEEE Trans. Antennas Propagat.*, Vol. 39, No. 1, 62–67, 1991.
22. Bradley, J., P. Collins, J. Fortuny-Guash, M. Hastriter, G. Nesti, A. Terzuoli, and K. Wilson, "An investigation of bistatic calibration techniques," *IEEE Trans. Geosci. Remote Sens.*, Vol. 43, No. 10, 2185–2191, 2005.
23. Eyraud, C., J.-M. Geffrin, A. Litman, P. Sabouroux, and H. Giovannini, "Drift correction for scattering measurements," *Appl. Phys. Lett.*, Vol. 89, No. 24, 244104, 2006.
24. Gilmore, C., P. Mojabi, A. Zakaria, M. Ostadrahimi, C. Kaye, S. Noghanian, L. Shafai, S. Pistorius, and J. LoVetri, "A wideband microwave tomography system with a novel frequency selection procedure," *IEEE Trans. Biomed. Eng.*, Vol. 57, 894–904, 2010.
25. Crocco, L. and A. Litman, "On embedded microwave imaging systems: Retrievable information and design guidelines," *Inverse Problems*, Vol. 25, No. 6, 065001, 2009.
26. Paulides, M., J. Bakker, N. Chavannes, and G. van Rhoon, "A patch antenna design for application in a phased-array head and neck hyperthermia applicator," *IEEE Trans. Biomed. Eng.*, Vol. 54, No. 11, 2057–2063, 2007.
27. Meaney, P., S. Pendergrass, M. Fanning, D. Li, and K. Paulsen, "Importance of using a reduced contrast coupling medium in 2D microwave breast imaging," *Journal of Electromagnetic Waves and Applications*, Vol. 17, No. 2, 333–355, 2003.
28. Franchois, A., "Contribution à la tomographie microonde: Algorithmes de reconstruction quantitative et vérifications experimentales," Ph.D. Thesis, University of Paris XI, Orsay, France, 1993.
29. Franchois, A. and A. G. Tijhuis, "A quasi-Newton reconstruction algorithm for a complex microwave imaging scanner environment," *Radio Sci.*, Vol. 38, No. 2, 8011, 2003.
30. Van den Berg, P. M. and J. T. Fokkema, "Removal of undesired wavefields related to the casing of a microwave scanner," *IEEE Trans. Microwave Theory and Tech.*, Vol. 51, No. 1, 187–192, 2003.
31. Lencrerot, R., "Outils de modélisation et d'imagerie pour un scanner micro-onde: Application au contrôle de la teneur en eau d'une colonne de sol," Ph.D. Thesis, Univ. P. Cezanne, Marseille,

France, 2008.

32. Bucci, O. M. and T. Isernia, "Electromagnetic inverse scattering: Retrievable information and measurement strategies," *Radio Sci.*, Vol. 32, No. 6, 2123–2138, 1997.
33. Fang, Q., P. Meaney, S. Geimer, A. Streltsov, and K. Paulsen, "Microwave imaging reconstruction from 3D fields coupled to 2D parameter estimation," *IEEE Trans. Medical Imaging*, Vol. 23, No. 4, 475–484, 2004.
34. Eyraud, C., A. Litman, A. Hérique, and W. Kofman, "Microwave imaging from experimental data within a Bayesian framework with realistic random noise," *Inverse Problems*, Vol. 25, No. 2, 024005, 2009.